LEUPHANA
UNIVERSITÄT LÜNEBURG

Experimental-numerical study of laser-shock-peening-induced retardation of fatigue crack propagation in Ti-17 titanium alloy

Sun, Rujian; Keller, Sören; Zhu, Ying; Guo, Wei; Kashaev, Nikolai; Klusemann, Benjamin

Published in:
International Journal of Fatigue

DOI:
10.1016/j.ijfatigue.2020.106081

Publication date:
2021

Document Version
Publisher's PDF, also known as Version of record

Link to publication

Citation for pulished version (APA):
Sun, R., Keller, S., Zhu, Y., Guo, W., Kashaev, N., & Klusemann, B. (2021). Experimental-numerical study of laser-shock-peening-induced retardation of fatigue crack propagation in Ti-17 titanium alloy. *International Journal of Fatigue*, *145*, Article 106081. https://doi.org/10.1016/j.ijfatigue.2020.106081

General rights
Copyright and moral rights for the publications made accessible in the public portal are retained by the authors and/or other copyright owners and it is a condition of accessing publications that users recognise and abide by the legal requirements associated with these rights.

- Users may download and print one copy of any publication from the public portal for the purpose of private study or research.
- You may not further distribute the material or use it for any profit-making activity or commercial gain
- You may freely distribute the URL identifying the publication in the public portal ?

Take down policy
If you believe that this document breaches copyright please contact us providing details, and we will remove access to the work immediately and investigate your claim.

Download date: 04. Dez.. 2025

International Journal of Fatigue 145 (2021) 106081

Contents lists available at ScienceDirect

International Journal of Fatigue

journal homepage: www.elsevier.com/locate/ijfatigue

Experimental-numerical study of laser-shock-peening-induced retardation of fatigue crack propagation in Ti-17 titanium alloy

Rujian Sun [a,b,c], Sören Keller [d,*], Ying Zhu [c], Wei Guo [c], Nikolai Kashaev [d], Benjamin Klusemann [d,e]

[a] Aeronautical Key Laboratory of Advanced Surface Engineering Technology, AVIC Manufacturing Technology Institute, Beijing 100024, China
[b] Science and Technology on Power Beam Processes Laboratory, AVIC Manufacturing Technology Institute, Beijing 100024, China
[c] School of Mechanical Engineering and Automation, Beihang University, Beijing 100191, China
[d] Institute of Materials Research, Materials Mechanics, Helmholtz-Zentrum Geesthacht, Max-Planck-Straße 1, 21502 Geesthacht, Germany
[e] Institute of Product and Process Innovation, Leuphana University of Lüneburg, Universitätsallee 1, 21335 Lüneburg, Germany

ARTICLE INFO

Keywords:
Laser shock peening
Residual stress
Fatigue crack propagation
Numerical simulation
Stress intensity factor
Ti-17 titanium alloy

ABSTRACT

Residual stresses induced by laser shock peening in Ti-17 titanium specimens were experimentally and numerically investigated to identify the mechanisms and generation conditions of the retardation of fatigue crack propagation (FCP). The retardation was experimentally observed with fatigue life prolonged by 150%. A multi-step simulation strategy for fatigue life prediction is applied, which successfully predicts the experimentally observed FCP behavior. The fractographic observations and numerical simulation indicate that crack closure, as opposed to other microstructural influences, is the dominant effect on retardation. The studies of multi-FCP aspects show that significant retardation occurs in specimens at high values of residual stresses, small peening gap distances, and lower externally applied loads.

1. Introduction

Titanium alloys have been widely used in aero engines, such as fan blades, blisks, and low-temperature section components of pressure compressors because of their high specific strength, excellent fatigue and high temperature oxidation properties, and corrosion resistance [1–4]. However, blades made of titanium are commonly thin wall structures with a variable cross section, are prone to severe mechanical and thermal coupled loads [5–7], and potentially suffer from foreign object damage [8–10] during operation. Once the damage is generated, the fatigue crack propagation (FCP) resistance becomes an important issue. A number of surface treatment techniques are used to improve FCP resistance and performance of load-bearing structures, such as shot peening [11,12], deep rolling [13,14], and laser shock peening (LSP) [15–17]. Of these, LSP employs a flexible laser medium that provides high controllability of the process [18], allowing for a locally optimized treatment without the need for tool changes. LSP is highly capable of introducing deep and high-value compressive residual stresses below the surface [19,20], which can reach 5–10 times deeper than in the case of shot peening [21,22]. Such deep penetrating compressive residual stresses are effective in improving fatigue properties by decelerating the crack propagation rate [23–25].

Van Aswegen and Polese [26], Kashaev et al. [27], and Hu et al. [28] experimentally demonstrated the effectiveness of compressive residual stresses on fatigue retardation, while Pavan et al. [29] and Busse et al. [30] investigated its effectiveness by numerical modeling: they all reported a significant FCP rate reduction inside the laser-peened area for aluminum alloys. In this regard, Pavan et al. [29] and Busse et al. [30] employed a two-dimensional finite element (FE) model based on experimentally determined residual stresses to investigate the FCP rate. In contrast, Keller et al. developed a three-dimensional multi-step simulation strategy from the LSP process simulation to the final FCP rate prediction [31], linking fatigue crack retardation to crack closure phenomena [32]. This multi-step simulation is applied and experimentally validated for the aluminum alloy AA2024. The authors identified crack closure as a dominant mechanism based on experimental fracture surface observations, combined with the numerical analysis. Such crack closure phenomena occur locally at the sites of high compressive residual stresses, meaning that residual stress distribution has a major influence on the resulting FCP behavior. Therefore, the specimen geometry influences the fatigue crack propagation, as the developing residual stresses depend on

* Corresponding author.
E-mail address: Soeren.Keller@hzg.de (S. Keller).

https://doi.org/10.1016/j.ijfatigue.2020.106081
Received 11 August 2020; Received in revised form 26 November 2020; Accepted 30 November 2020
Available online 15 December 2020
0142-1123/© 2020 The Author(s). Published by Elsevier Ltd. This is an open access article under the CC BY license (http://creativecommons.org/licenses/by/4.0/).

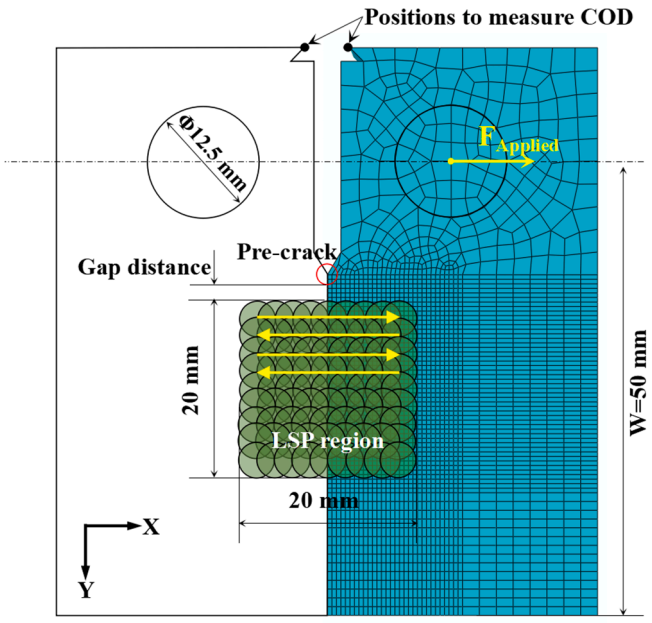

Fig. 1. Schematic of C(T) specimen with the peening zone indicated and the spatial discretization of the three-dimensional FE C(T) specimen model.

the specific specimen geometry. In addition to the mentioned studies on aluminum alloys, our previous experimental research demonstrates similar characteristic retardation in laser-peened Ti-17 [33] specimens, raising the question of a cross-material explanation of the LSP-induced fatigue crack retardation. This is particulary relevant, because it is still under debate how dominant possible microstructure effects (i.e. material crystal structure, grain orientation, grain size distribution) are. Although it is shown that residual stresses causing crack closure are the main mechanisms to retard the FCP in AA2024, this conclusion has not been transferred to another material system yet. A thorough understanding of retardation is of great importance and necessary for a damage-tolerant design and for the extension of fatigue life. This can only be reached by a holistic numerical approach, considering in particular also the LSP-characteristic residual stress over-the-depth profiles via a three-dimensional simulation approach to predict the FCP retardation.

The present study seeks to understand the retardation mechanisms of fatigue cracks by LSP-induced residual stresses in Ti-17 titanium alloy and to identify beneficial peening conditions for FCP retardation. Therefore, a multi-step three-dimensional numerical simulation strategy is adopted for the used laser system and applied for the first time to Ti-17 to predict the FCP rate influenced by the laser peening process, i.e. peening patch position and varying residual stresses, as well as the external applied loads. The LSP process simulation is adjusted to the used high-energy laser system based on the experimentally determined residual stresses. The subsequent FCP rate predictions are experimentally validated for Ti-17 titanium alloy. Relevant material parameters for the FCP rate prediction are determined in the unpeened material and applied to the peened specimen. This experimental and numerical study aims to reveal the FCP retardation mechanisms in LSP-treated Ti-17 to expand the LSP applications in scientific and engineering fields.

2. Material and experiments

2.1. Material

Ti-17 (Ti-5Al-2Sn-2Zr-4Mo-4Cr) titanium alloy plates, having a thickness of 5 mm, acquired from BAOTI Group Co., Ltd., were used in this study. The material underwent a solution heat treatment (840 °C × 1 h, air cooling + 800 °C × 4 h water quenching) and aging (630 °C × 4 h, air cooling), showing a final microstructure of equiaxed α- and β-phase grains.

2.2. LSP experiments

LSP experiments were carried out at AVIC Manufacturing Technology Institute on a Q-switched Nd: YAG high power-pulsed laser system with a wavelength of 1064 nm, a pulse duration of 15 ns (FWHM), a circular spot size of 4 mm, and an overlapping ratio of 50%. The employed laser pulse energy was 25 J, corresponding to a power density of 13.26 GW/cm^2. Prior to LSP, a 100-μm-thick aluminum foil, manufactured by Minnesota Mining and Manufacturing (3 M, USA), was attached to the peening surface to avoid possible damage or roughening of the irradiated surface, and to reduce the reflection loss of the incident laser pulse. During LSP, a running deionized water layer with a thickness of 1–2 mm was applied as a transparent constrained layer to increase the peak pressure of the laser-induced shock wave. Specimens were double-side peened with a zigzag laser path covering an area of approximately 20 mm × 20 mm, as shown in Fig. 1. These peening parameters are chosen to generate residual stresses, which lead to significant FCP retardation without causing global specimen deformation and at the same time providing a high surface quality. The chosen high overlapping ratio guarantees a complete surface irradiation, leading to more homogeneous residual stresses parallel to the surface plane. Furthermore, the parameters are chosen in such a way as to introduce residual stresses with values below 80% of material yield strength, which would otherwise require a correction of the experimentally determined values due to plastic deformation [34].

2.3. FCP tests

FCP tests were performed on a fatigue testing system (Instron 8801-50 kN, USA), using compact tension (C(T)) specimens, in line with the Chinese national standard GBT 6398-2000 (similar to ASTM E647-15). The width of the C(T) specimens was 50 mm, see Fig. 1. The C(T) specimens were first pre-cracked to approximately 14.0 mm (1.5 mm from the notch tip) under mode-I loading (tensile opening), with constant amplitude loading, using the maximum force of 2.22 kN and a stress ratio of 0.1. The tested C(T) specimens are divided into BM (base metal) and LSPed (laser shock peened) specimens. The peening zone in the LSPed specimens was placed in front of the pre-crack, i.e. gap distance 0.0 mm, where the columns of the zigzag path of the LSP sequence were perpendicular to the crack propagation direction. Afterward, the C(T) specimens were tested, applying a sinusoidal load at a frequency of 20 Hz, having a maximum force of 1.67 kN and a stress ratio of 0.1 at ambient temperature (20 °C) in air. The length of the fatigue crack was determined by a crack opening displacement (COD) gauge attached to the specimen (the measuring positions are shown in Fig. 1). The range of the applied stress intensity factor (SIF) without influencing residual stresses (ΔK_{nRS}) is determined according to ASTM E647-15:

$$\Delta K_{nRS} = \frac{\Delta P}{B\sqrt{W}} Y \ , \tag{1}$$

where $\Delta P = P_{max} - P_{min}$ is the external load range, B is the specimen thickness, and W is the width of the specimen. Y represents a geometrical factor given by ASTM E641-15:

$$Y = \frac{2+[a/W]}{[1-[a/W]]^{3/2}}\left[0.886+4.64\left[\frac{a}{W}\right]-13.32\left[\frac{a}{W}\right]^2+14.72\left[\frac{a}{W}\right]^3-5.60\left[\frac{a}{W}\right]^4\right], \tag{2}$$

where a is the current crack length. After failure, the fracture surfaces were investigated using a scanning electron microscope (SEM, Carl Zeiss-Gemini 500, Germany) with an accelerating voltage of 15 kV. The crack length a of the specimen is calculated based on the compliance of the specimen by

$$a/W = C_0 + C_1 U_x + C_2 U_x^2 + C_3 U_x^3 + C_4 U_x^4 + C_5 U_x^5 \tag{3}$$

with

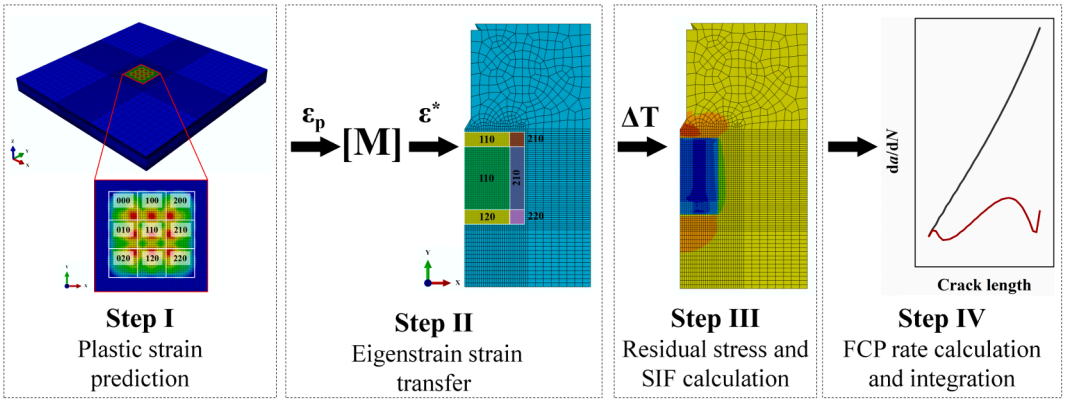

Fig. 2. Multi-step strategy for transferring residual stress into the C(T) specimen, following the approach of Keller et al. [31].

$$U_x = \frac{1}{\sqrt{\frac{BE(\Delta COD)}{\Delta P}} + 1}, \tag{4}$$

where E is Young's modulus, ΔCOD is the crack opening displacement measured at the crack mouth, and C_i denotes regression coefficients, see [35].

2.4. Residual stress analysis

We determined the residual stresses within the C(T) specimens following the incremental hole-drilling method, using the PRISM measurement system from StressTech, Finland. PRISM is equipped with an optical-electronic speckle pattern interferometer system, providing high-quality full-field data for accurate residual stress calculation. A detailed description of this technique is provided by Steinzig and Ponslet [36–39]. In this study, residual stresses from both sides of the specimen were determined up to a depth of 1.1 mm, using a driller with a diameter of 3.2 mm. The drilling increment was 0.05 mm near the surface, where high residual stress gradients are expected, and it was increased up to 0.2 mm at a depth of around 1 mm. Each residual stress determination was performed five times for each specimen to obtain sufficient statistics.

3. Numerical simulation methodology

3.1. Multi-step simulation approach

Following the work of Keller et al. [31], a multi-step simulation approach is used to predict the FCP rate influenced by LSP-induced residual stresses, see Fig. 2. First, an LSP process simulation is used to predict the plastic strain within a representative volume, which is significantly smaller than the peened area on the C(T) specimen (Step I). The plastic strains due to the LSP-induced residual stresses are then stored in a matrix (M). Subsequently, these strains are introduced to the C(T) specimen as thermal strains in line with the eigenstrain approach [21,40,41] (Step II). The residual stress distribution within the C(T) specimen and the SIFs at the crack front are predicted for different crack lengths and external loads (see Step III). Based on the calculated SIFs, the FCP rate is determined by a well-known fatigue crack propagation model, i.e. Paris's law in the current study (see Step IV). Subsequently, the FCP rate can be integrated to calculate the number of cycles until a specific crack length is reached.

3.2. LSP process simulation and plastic strain transfer

The first step of the multi-step simulation approach consists of the LSP process simulation, which is conducted with 4 × 4 shots in the center of the three-dimensional FE model with a size of 60 mm × 60 mm × 5 mm in ABAQUS, see Fig. 3. A double bias mesh was used in the depth direction with element size ranging from 0.02 mm on the top and bottom surface to 0.05 mm in the middle section, see Fig. 3a, leading to a mesh-independent solution. Three-dimensional continuum elements with reduced integration (element type C3D8R) are used. The model boundaries at the x–z and y–z planes are fixed, as depicted in Fig. 3. The peened surfaces are modeled as free surfaces. An elastic-viscoplastic material behavior is assumed, where the elastic material behavior is modelled as being linear with Young's modulus E = 115 GPa and

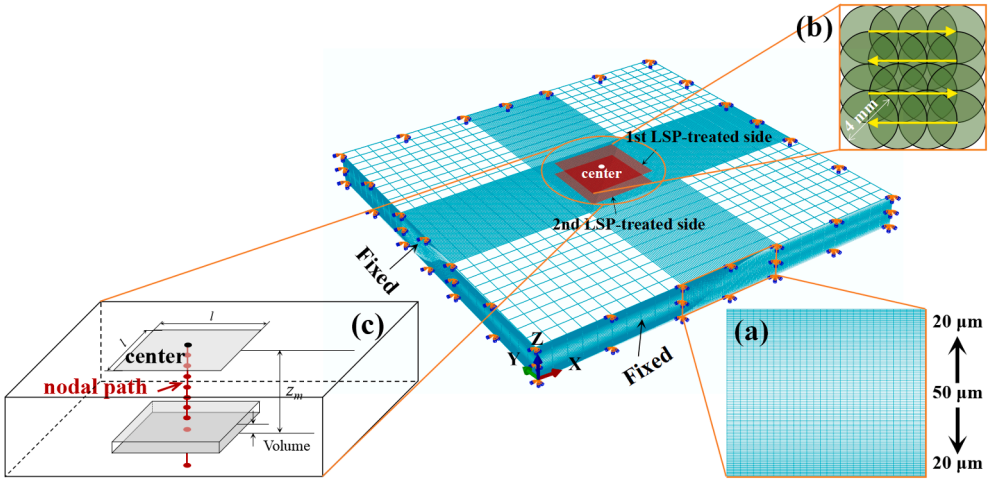

Fig. 3. LSP process model to predict the plastic deformation in a representative volume. (a) Double bias mesh design, (b) zigzag laser path with an overlapping ratio of 50%, (c) schematic of the averaging volumes and the nodal path used to evaluate the residual stresses.

Table 1
Physical and mechanical properties of Ti17 titanium alloy employed in the simulation in this study.

Quantity	Symbol	Value	Unit	Reference
Density	ρ	4650	kg/m^3	–
Young's modulus	E	115	GPa	–
Poisson's ratio	ν	0.33	–	–
Static yield strength	A_{JC}	1100	MPa	[43]
Strain hardening coefficient	B_{JC}	590	MPa	[43]
Strain hardening exponent	n	0.41	–	[43]
Strain rate hardening parameter	C_{JC}	0.0152	–	[43]
Reference strain rate	$\dot{\varepsilon}_{p,0}$	1	s^{-1}	–

Poisson's ratio $\nu = 0.33$. The reduced Johnson-Cook constitutive model [42]

$$\sigma_Y = \left[A_{JC} + B_{JC}\varepsilon_p^n\right]\left[1 + C_{JC} ln\left(\frac{\dot{\varepsilon}_p}{\dot{\varepsilon}_{p,0}}\right)\right] \quad (5)$$

is employed to account for the viscoplastic material behavior at the high strain rates (up to 10^6 s^{-1}) during the LSP process. Here, A_{JC} represents the static yield strength, B_{JC} the strain-hardening coefficient, n the strain-hardening exponent, C_{JC} the strain rate hardening parameter, and $\dot{\varepsilon}_{p,0}$ the reference strain rate. The material parameters employed in this study for Ti-17 are summarized in Table 1. A VDLOAD Fortran subroutine was used to apply the pressure loading of the laser impacts considering the zigzag laser path, as shown in Fig. 3b. Fig. 3b illustrates the schematic path for evaluating the nodal stresses at the center line, starting at the first LSP-treated side and ending at the second LSP-treated side. Besides, the method of averaging volume stresses, which calculates the mean stress value via an averaging volume, is illustrated in Fig. 3c. The size of the averaging volume is chosen 3 mm × 3 mm × 0.25 mm in projection.

The temporal distribution of the applied pressure is simplified into a 30 ns rectangular pulse. The spatial distribution of the pressure represents a typical Gaussian distribution. The pressure pulse parameters were adjusted to match the experimentally determined residual stresses in the C(T) specimen. Thus, the adjusted pressure pulse might not represent a physically correct temporal pressure distribution, which is also unknown; however, the adjusted pressure pulse causes the same plastic deformation of the material as the physically correct pressure pulse. Such identified pressure pulse is transferable to different peening sequences and similar materials, as shown for several aluminum alloys by the authors [31,44]. Numerically predicted local residual stresses are averaged in representative volumes at the respective depths to enable a comparison to experimentally determined residual stresses, which also represent experimentally the average stress of a certain volume in a certain depth. For further details, the interested reader may refer to Keller et al. [44]. The importance of stress averaging is shown by comparison with the local stress distribution, see Section 4.1.

The LSP process simulation of a relatively small area of 4 × 4 shots allows the calculation of the plastic strains (ε_p) inside a representative volume. This is based on the assumption that further LSP shots next to the present pattern will not influence the plastic strains within this representative volume. The plastically affected volume of the LSP process simulation was divided into several units according to their specific positions, as illustrated in Fig. 2, see Step I. The determined plastic strains were averaged in each unit and stored in the matrix [M]. In line with the eigenstrain approach, these strains are applied to the C(T) specimen as thermal strains, assuming periodicity. Hence, the plastic strains of the relatively small area of 4 × 4 shots can be extrapolated to the relatively large area of 9 × 9 shots or even more, leading to a significant decrease in computational costs. A combination of specific thermal expansion coefficients for each unit and a temperature increase was applied to reach the desired thermal strains, which correspond to the plastic strains of the LSP process simulation. After relaxation, these result in the intended residual stress distribution within the C(T) specimen, see Step II.

3.3. Calculation of SIF and FCP rate

Half of the C(T) specimen is modeled by applying symmetry boundary conditions along the crack path, and linear elastic material behavior is adopted. The element size along the symmetry plane is about 0.25 mm. To model crack propagation, the symmetry conditions are released depending on the crack length and replaced by contact conditions to a rigid plate, see Fig. 4a. A hard contact in the normal direction and frictionless contact conditions in the tangential direction is assumed. The contact between the C(T) specimen and the rigid plate simulates crack face contact. A straight crack front perpendicular to the surfaces is assumed. As shown in Fig. 4b, the external loading is applied at the central nodes of the pin. The pin is modeled as a section of the C(T) specimen to avoid contact modelling between pin and specimen. To simulate a realistic loading of the specimen, the pin is split into two parts, exhibiting a different stiffness, see Fig. 4b. Hence, the right part of the pin contains a relatively high stiffness and the left part of the pin exhibits a relatively low stiffness. It has to be mentioned that the

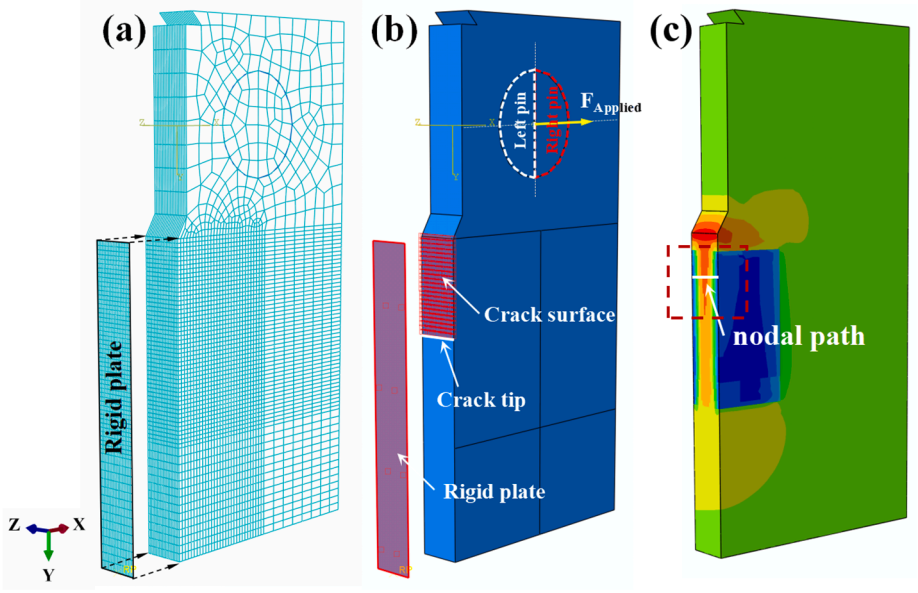

Fig. 4. The spatially discretized FE model of the half C(T) specimen is depicted in (a). Crack face contact is modelled as contact conditions to a rigid plate placed in the symmetry plane, see (b). The three-dimensional residual stress field introduced by the eigenstrain method shows a high gradient in depth direction but neglects the residual stress variations parallel to the surface, as illustrated in (c). Therefore, the residual stresses below the peened area of the C(T) specimen are evaluated along the depicted node path in the following. The force that is applied to the implicitly modeled pin (with different stiffness for both parts) acts in the x-direction, representing pure mode-I loading.

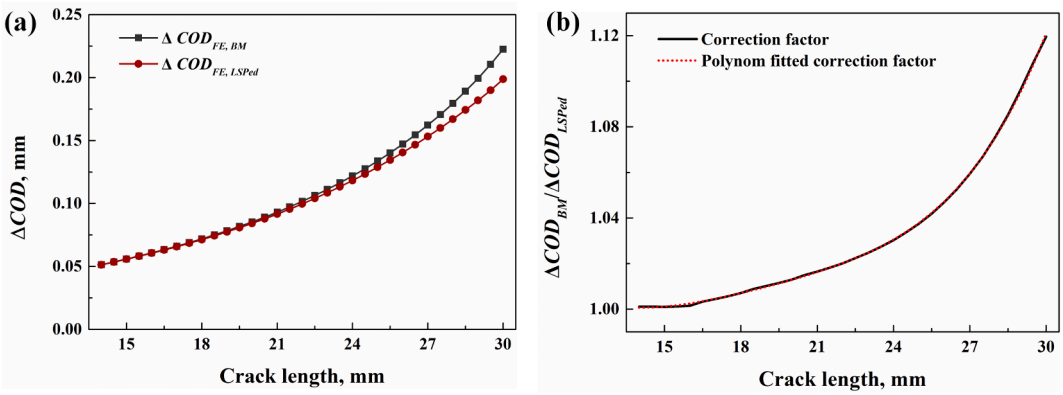

Fig. 5. ΔCOD vs. crack length a curves, determined by FE simulations, are depicted in (a). Crack closure leads to a difference of the ΔCOD for peened and unpeened specimens, leading to uncertainty about the crack length calculation during the FCP experiment. The ratio of ΔCOD for unpeened and peened specimens over the crack length a can be used to correct the uncertainty of the crack length prediction. Here, the ΔCOD ratio determined by FE simulations is approximated by a polynomial of the fourth order, see (b).

resulting SIFs are independent of the specific pin modelling approach. Residual stress profiles in the z-direction of the C(T) specimen were determined node-wise along the nodal path illustrated in Fig. 4c. The residual stresses within the model of the C(T) specimen do not show high local variations in x- and y-directions, due to the introduced averaged eigenstrains, as described in the previous section. Disregarding the local variation in residual stress implies a simplification of the physical crack propagation conditions, but it is found to be valid for LSPed AA2024 and applied for Ti-17 in this work.

The actual SIF K_{cd}, which describes the crack-driving SIF, is determined via the crack-closure technique based on the nodal displacements and forces calculated at the crack front [45]. The elemental energy release rate G^J_{ele} of the J^{th} element along the crack path is determined via

$$G^J_{ele} = \frac{1}{2b^J_{ele}\Delta a}\sum_{j=1}^{2} C^j u^j_z F^j_z \ , \tag{6}$$

where b^J_{ele} denotes the thickness of the J^{th} element along the crack path, Δa is the crack extension, F^j_z is the nodal reaction forces at the element, u^j_z is the nodal displacements of the nodes at the crack front. Eq. (6) holds for elements with two nodes along the crack front. C^j represents weighting factors, taking the thickness of the current and adjacent elements into account:

$$C^1 = \frac{b^J_{ele}}{b^J_{ele} + b^{J-1}_{ele}} \text{ and } C^2 = \frac{b^J_{ele}}{b^{J+1}_{ele} + b^J_{ele}} \ . \tag{7}$$

The SIF of the whole crack front is finally calculated by averaging the element SIF K_{ele}

$$K^J_{ele} = \sqrt{E' G^J_{ele}} \text{ and } K_{cd} = \frac{1}{N_{ele}}\sum_{J=1}^{N_{ele}} K^J_{ele} \ , \tag{8}$$

where N_{ele} is the number of elements along the crack front and E' is the modified Young's modulus, with $E' = E$ for plane stress and $E' = E(1-\nu^2)^{-1}$ for plane strain conditions. The SIF K_{cd} accounts for the combined loading of residual and applied stresses. Where no residual stresses are present, K_{cd} corresponds to K_{nRS}. A detailed description of the element-wise calculation of the SIF can be found in [46].

After obtaining the maximum and minimum crack-driving SIFs, $K_{cd,\max}$ and $K_{cd,\min}$, the SIF range $\Delta K_{cd} = K_{cd,\max} - K_{cd,\min}$ at different crack lengths can be calculated. According to Paris's law [47], the FCP rate (da/dN) during cyclic loading can be determined via

$$da/dN = C_p[\Delta K_{cd}]^m \ , \tag{9}$$

where C_p and m are material-specific constants obtained from base material tests. The FCP rate for the C(T) specimen is predicted for crack lengths between $a = 14$ mm and $a = 30$ mm. Thus, the crack front is located in the peened region, see Fig. 1, and the fatigue crack should be strongly influenced by LSP-induced compressive residual stresses during the entire FCP test. Keller et al. [31] showed that the FCP in the LSP-treated region, containing high compressive residual stresses, is mainly influenced by ΔK_{cd}. Hence, Paris's law is assumed to be sufficient to predict the FCP rate in this investigation. If significant tensile residual stresses are present in front of the crack tip, the NASGRO equation is more appropriate to describe the crack propagation behavior, but it also requires the identification of more material parameters. Since this work mainly focuses on the region of high compressive residual stresses, the application of Paris's law is assumed to be sufficient to describe the FCP behavior.

3.4. Crack-length correction of the LSP-treated specimens

C(T) specimens indicate crack closure in regions of high compressive residual stresses. Crack closure caused by the compressive residual stresses influences the measured ΔCOD, see Fig. 5a. The changed ΔCOD leads to an error of the calculated crack length based on Eqs. (3) and (4). This error, induced by crack closure phenomena, is corrected based on the FE simulation of the C(T) specimen. The FE simulation of the C(T) specimen is used to calculate the actual ΔCOD, corresponding to the crack length for the unpeened ($\Delta COD_{FE,BM}$) and peened specimens ($\Delta COD_{FE,LSPed}$). Thereafter, a correction function f_{cor} is determined based on a polynomial fit of the fourth order:

$$\frac{\Delta COD_{FE,BM}(a)}{\Delta COD_{FE,LSP}(a)} = f_{cor}(a) = D_0 + D_1 a + D_2 a^2 + D_3 a^3 + D_4 a^4 \tag{10}$$

where D_i is determined by linear regression ($R^2 = 0.99981$): $D_0 = 1.5273$, $D_1 = -1.1370{\cdot}10^{-1}$, $D_2 = 9.0155{\cdot}10^{-2}$, $D_3 = -3.1404{\cdot}10^{-5}$, $D_4 = 4.1604{\cdot}10^{-6}$, see Fig. 5b. This function allows the correction of the experimental determined $\Delta COD_{LSPed,exp}$ for peened specimens with

$$\Delta COD_{cor,exp} = \Delta COD_{LSPed,exp}\ f_{cor}(a) \ . \tag{11}$$

The corrected $\Delta COD_{cor,exp}$ is used in Eqs. (3) and (4) to determine the real crack length in the experiments on the peened specimen. It has to be noted that the function is unique on the considered interval 15 mm $< a <$ 30 mm. The underlying assumption is that the ΔCOD ratio of the base material and of the peened specimens in experiments and numerical simulations is identical:

$$\frac{\Delta COD_{FE,BM}(a)}{\Delta COD_{FE,LSPed}(a)} = \frac{\Delta COD_{exp,BM}(a)}{\Delta COD_{exp,LSPed}(a)} \ . \tag{12}$$

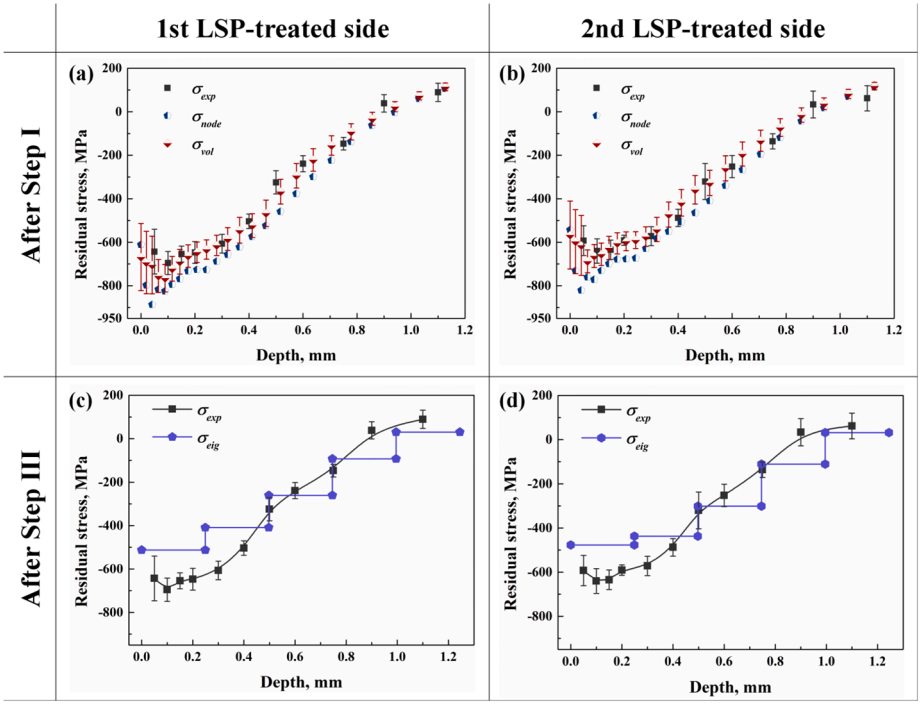

Fig. 6. Residual stresses obtained from the experiments σ_{exp} and for the simulations after the LSP process simulation, i.e. Step I (nodal stress σ_{node} and volume-averaged stress σ_{vol}) on the first LSP-treated side (a) and the second LSP-treated side (b), are shown. (c) and (d) show the comparison of the resulting residual stress distribution after the application of the eigenstrain method σ_{eig} (Step III) to the C(T) specimen with the experimentally determined residual stresses. All residual stress distributions show the stress component in x-direction (perpendicular to the crack propagation direction) and are determined after the LSP treatment of both material sides.

4. Results and discussion

4.1. Residual stress comparison

Fig. 6 shows the experimental (σ_{exp}) and numerically determined residual stress distributions in depth direction within the peened area of the LSPed specimen. For completeness, the numerical stresses determined at the nodes (σ_{node}) on the center path, see Fig. 3a, as well as via volume averaging (σ_{vol}), are investigated. In the experiment, the σ_{exp} is obtained perpendicular to the crack propagation direction. The maximum compressive residual stress (700 MPa) is found on the first LSP-treated side, Fig. 6a, which is about 60 MPa higher than the maximum compressive stress on the second LSP-treated side, Fig. 6b. The maxima are present at a depth of around 0.1 mm from the surface. With increasing depth, the stress gradually decreases, and some tensile residual stresses appear in the middle section due to stress balance. The higher residual stresses on the first LSP-treated side are related to the fact that tensile residual stresses are generated on the second LSP-treated surface when peening the first side, which reduces the amount of compressive residual stress during the second side-peening step [48]. Good agreement between experiment and simulation in terms of the residual stresses is obtained, independent of the stress evaluation approach in the simulation, i.e. nodal or volume-average stress. However, the standard deviation at a specific depth can only be determined for the volume average stress σ_{vol}, which is calculated from all stress values in the specific averaging volume. The nodal stress values show some deviations from the experimental results near the surface, which may be related to the present high local residual stress gradients. Since the incremental hole-drilling method determines average stress, depending on the area of the measured surface displacements and drilled hole increment, a comparison is only valid in terms of the volume average stress σ_{vol}. High local stress gradients are reflected by a significant standard deviation of σ_{vol}, which decreases with increasing depth; hence, the nodal stress values also show good agreement deep within the material.

Fig. 6c and d expound the comparison between the experimentally determined residual stress σ_{exp} and the resulting residual stresses introduced by the eigenstrain method (σ_{eig}) in the C(T) specimen after Step III. σ_{eig} shows a step-wise distribution, where the width of each step corresponds to the chosen discretization size used for the plastic strain volume averaging and corresponding transfer, see Steps I and II in Fig. 2.

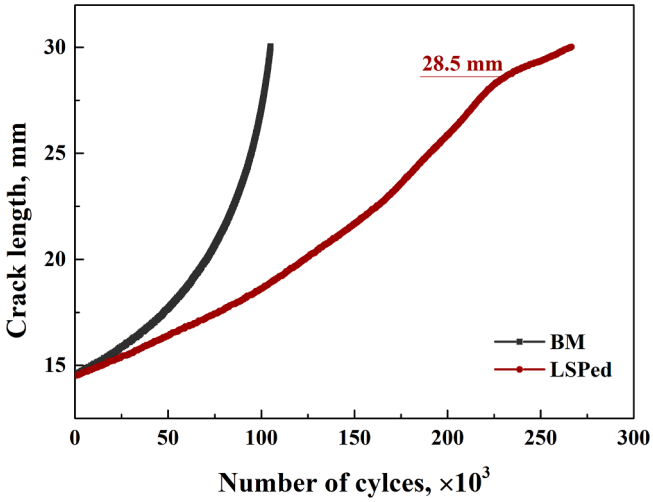

Fig. 7. The number of cycles as a function of the crack length in BM and LSPed specimens. The applied LSP treatment leads to a significant improvement in fatigue life in the LSPed specimen.

If necessary, the discretization size in the depth direction can be reduced, leading to smaller steps, i.e. a more accurate reproduction of σ_{vol} can be obtained, see Fig. A1. However, the current discretization already shows convergence for predicting the SIFs, see Appendix A.

4.2. FCP behavior

The evolving crack length over the number of cycles N is shown in Fig. 7. The fatigue life of the BM is estimated as 1.05×10^5 cycles, while the LSPed specimen withstands 2.66×10^5 cycles, i.e. an increase of 150% compared to the BM specimen. The lower FCP rate in the LSPed specimen is attributed to the compressive residual stresses near the crack tip. These minimize the actual local load due to crack closure, as indicated by SEM images and numerical simulation in the following, which is consistent with the observation of Keller et al. [32] for aluminum.

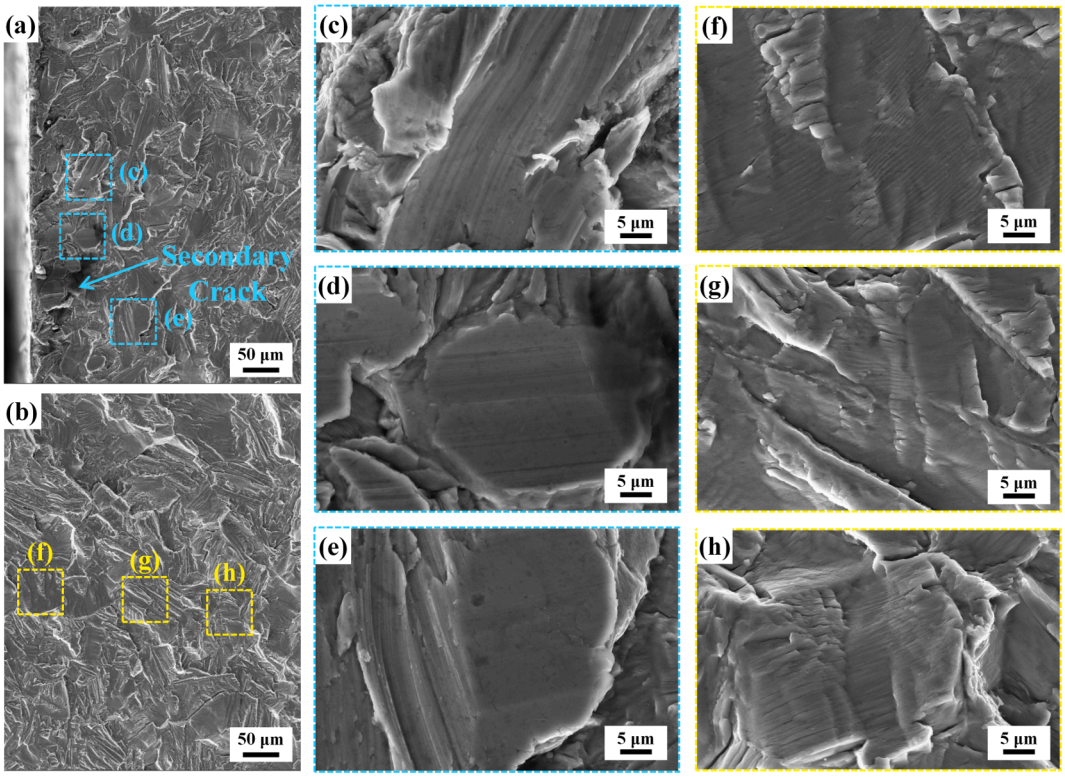

Fig. 8. SEM images of the fracture surface in the LSPed specimen, taken at a crack length of around 29 mm. (a), (c)–(e) show the near-surface area, in which the typical fatigue striations are missing with the observation of a plasticized fracture surface and secondary cracks due to the presence of crack closure. (b), (f)–(h) show the middle section area with the typical fatigue striations.

Fig. 8 shows the SEM images of the fracture surface observed at a crack length of 29 mm in the LSPed specimen, which details the morphological features of the near-surface and mid-thickness regions. The macrographs of the fracture surface next to the material surface (Fig. 8a) and at mid-thickness (Fig. 8b) show, no obvious differences. Both fracture surfaces are covered with a large number of tearing ridges. However, detailed analysis reveals significant differences. At the near-surface region there appear many plasticized flat surfaces and some secondary cracks, which may have originated from the close mechanical contact between the crack surfaces during crack propagation, Fig. 8c-e. In contrast, the mid-thickness region exhibits numerous parallel fatigue striations, which are traces resulting from the blunting and re-sharpening of the crack tip, Fig. 8f-h. Such differences are associated with the distinct residual stress state at the surface and the mid-thickness region. Owing to the compressive residual stress near the surface region, there are crack closure effects. The literature reports similar plasticized fracture surfaces after LSP treatment for aluminum [27,32], which is why crack closure is assumed to be the main cause of the different appearances of the fracture surfaces. This finding is supported by the numerical simulation in the following.

Fig. 9a shows the numerically obtained FCP rate da/dN from the multi-step simulation over the crack length a in comparison with the experimental results. The FCP rate of the BM specimen exhibits a continuous increase from 3.38×10^{-5} mm/cycle to 2.50×10^{-4} mm/cycle. The Paris parameter $C_P = 8.986 \times 10^{-8}$ and $m = 3.186$ are determined based on experiments of unpeened material. The FCP rate in the LSPed specimen still increases continuously due to the constant amplitude loading, but at a significantly low rate compared to the BM. The numerically predicted FCP rates in the LSPed specimens are in good agreement with the experimentally determined ones, see Fig. 9a.

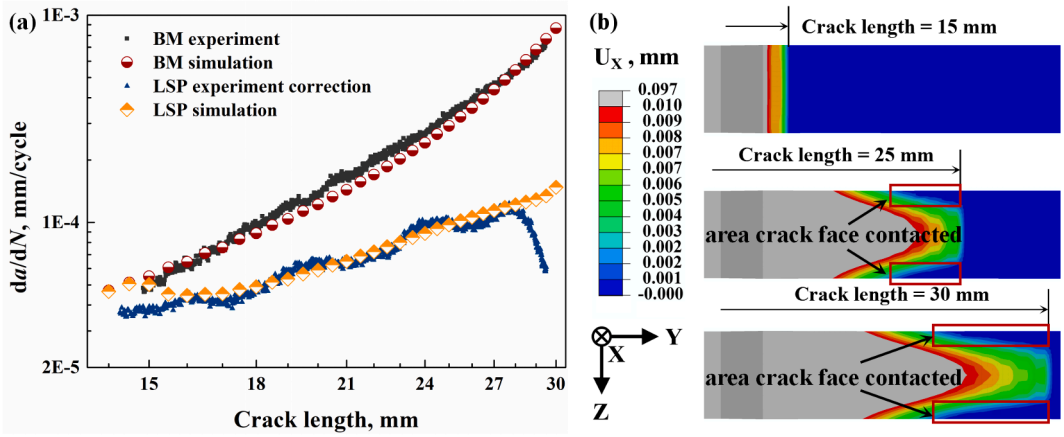

Fig. 9. (a) Comparison between the experimentally determined and numerically predicted FCP rate in the BM and LSPed specimens, and (b) crack surface displacement at different crack lengths and at minimum applied load.

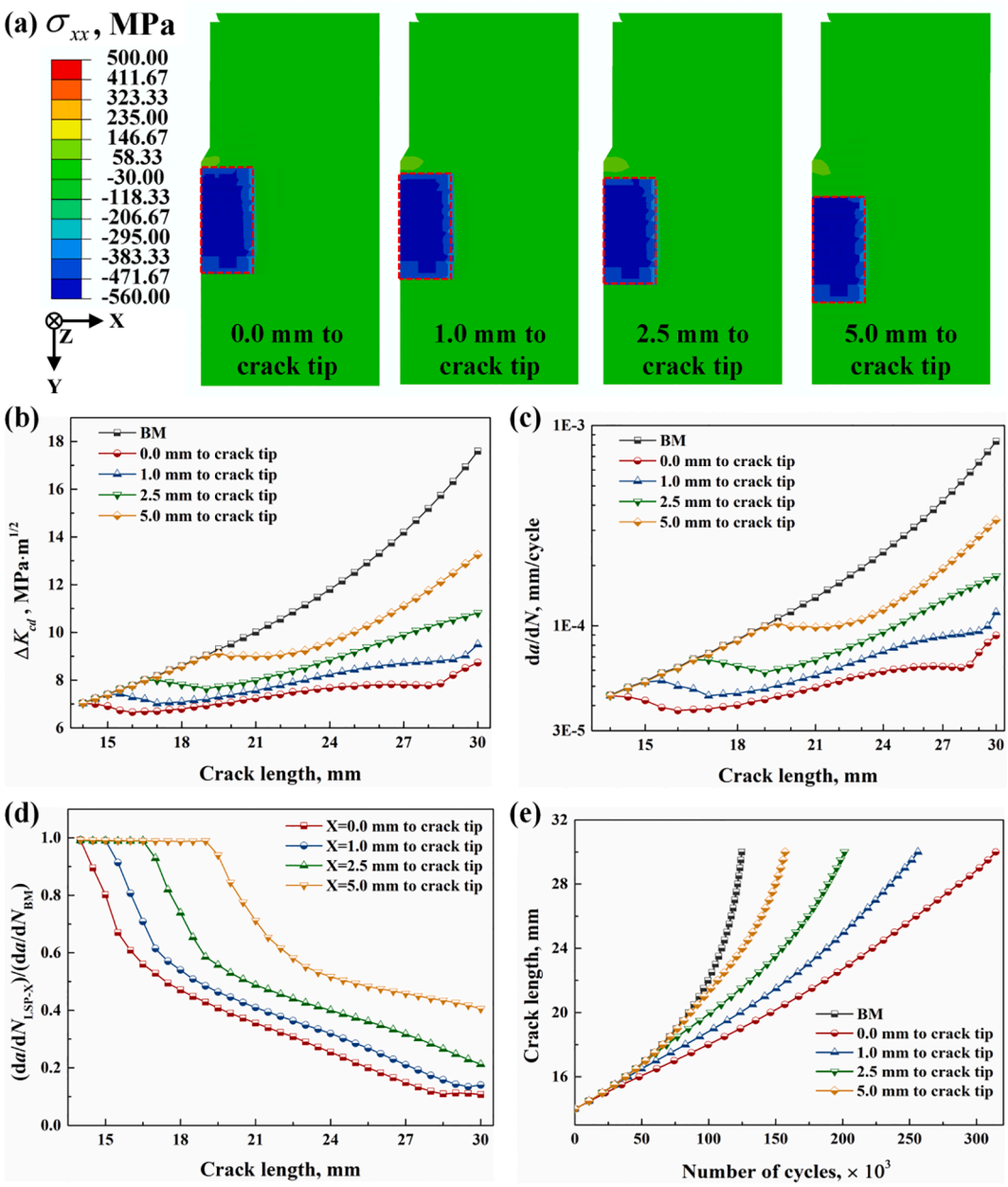

Fig. 10. Numerically obtained FCP behavior in specimens with different peening patch positions. The initial stress maps, illustrating the different peening patch positions, are shown in (a). The resulting SIF range ΔK_{cd} and FCP rate da/dN over the crack length for the different patch positions are displayed in (b) and (c), respectively. FCP retardation is investigated by the da/dN_{LSP,X_i} : da/dN_{BM} vs. crack length curves in (d). Finally, the total load cycle number is determined by integrating da/dN in (e).

Fig. 9b shows the displacement of the crack surface for crack lengths of 15 mm, 25 mm, and 30 mm. Crack closure, indicated by zero value displacements at the crack surface, is present near the peened surface in the region of high compressive residual stresses at the minimum applied load. This crack closure influences the stress distribution at the crack tip, leading to a lower SIF range. This lower SIF range results in a lower FCP rate in the LSPed specimen than the BM at the same crack length. The detected fatigue crack retarding mechanisms in Ti-17 correspond to those in AA2024 [32], suggesting a generalized cross-material explanation of the fatigue crack propagation influenced by LSP-induced residual stress fields. This indicates that, compared to the present residual stresses, microstructural effects, which obviously differ between the material systems, are not of significant relevance in terms of the resulting FCP behavior.

4.3. Influence of LSP design parameters on the resulting FCP rate

In this section, the multi-step simulation is used to investigate numerically important aspects of the LSP application in terms of the resulting fatigue performance, i.e. peening patch position, maximum of introduced residual stress, and the magnitude of the external applied loads.

4.3.1. Influence of the peening patch position

The effect of the peening patch position on the FCP behavior is investigated by varying the gap distance between the notch tip and the peening zone. Four different peening patch positions with gap distances of 0.0 mm, 1.0 mm, 2.5 mm, and 5.0 mm are simulated, see Fig. 10a. The SIF range ΔK_{cd} and the FCP rate (da/dN) as a function of the crack length are illustrated in Fig. 10b and c, respectively. To quantitatively compare the effect of the peening patch position, the retardation ratio da/dN_{LSP,X_i} : da/dN_{BM} is introduced by dividing the FCP rate of the BM

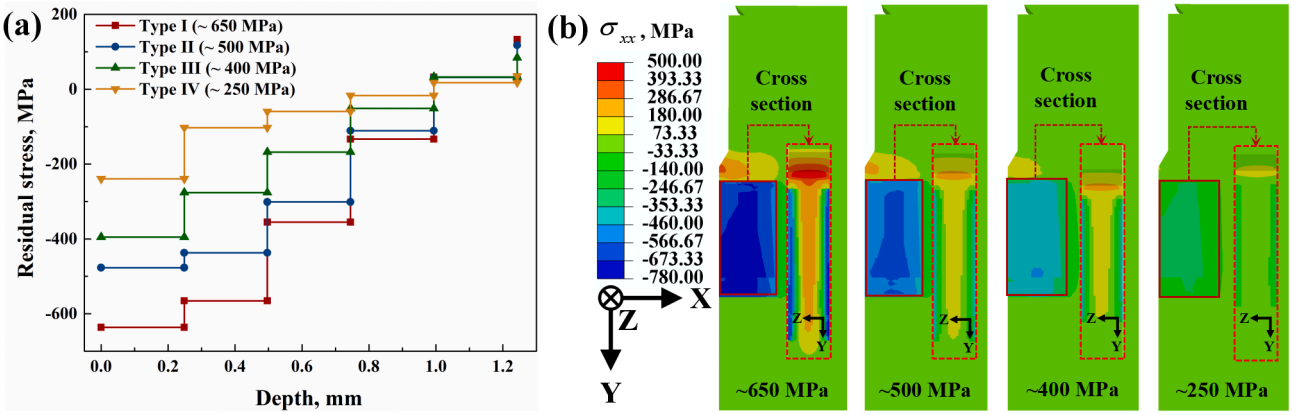

Fig. 11. Residual stress fields with four different maxima in terms of compressive residual stresses were introduced to the C(T) specimen via the eigenstrain approach, as illustrated in (a), where the spatial distribution of the residual stress component σ_{11} is shown in (b), including a cross-sectional view of the y–z plane.

specimen da/dN_{BM} with the FCP rate of the LSPed specimen $da/dN_{LSP,X_i}$, with X_i representing the specific gap distance, see Fig. 10d. The crack length a versus the number of load cycles N is determined by integrating the respective da/dN curves, Fig. 10e, showing a decrease in fatigue life with an increase in the peening patch gap distance.

Before entering the peening zone, all specimens show the same ΔK_{cd} as the unpeened specimen, see Fig. 10a. A decrease of ΔK_{cd} occurs in the peened region due to the presence of the introduced compressive residual stresses that cause crack closure. The FCP rate demonstrates that the LSP treatment close to the notch is beneficial to the overall fatigue life, which can be explained by two effects: (i) with a small gap distance, the retardation is present at a small crack length; (ii) the constant amplitude loading of the experiments causes an increasing FCP rate with increasing crack length because the SIF increases with the crack length as well. Therefore, small or no gap distance leads to the retardation of a slow-growing crack, which impacts the total cycle number more significantly than the retardation of an already fast-growing crack.

However, the FCP retardation is about the same inside the peening patch for the gap distances $x = 0$ mm, $x = 1$ mm, and $x = 2.5$ mm, see Fig. 10d. Thus, the LSP treatment has almost the same influence on the FCP retardation inside the peening patch. When the crack length is increased, slight differences in the FCP retardation ratio result from the increasing stress field next to the crack front. Therefore, the crack closure phenomena decrease slightly because the crack front loading increases, which is clearly observable by comparing the FCP retardation ratios for gap distances of 0 mm and 5 mm.

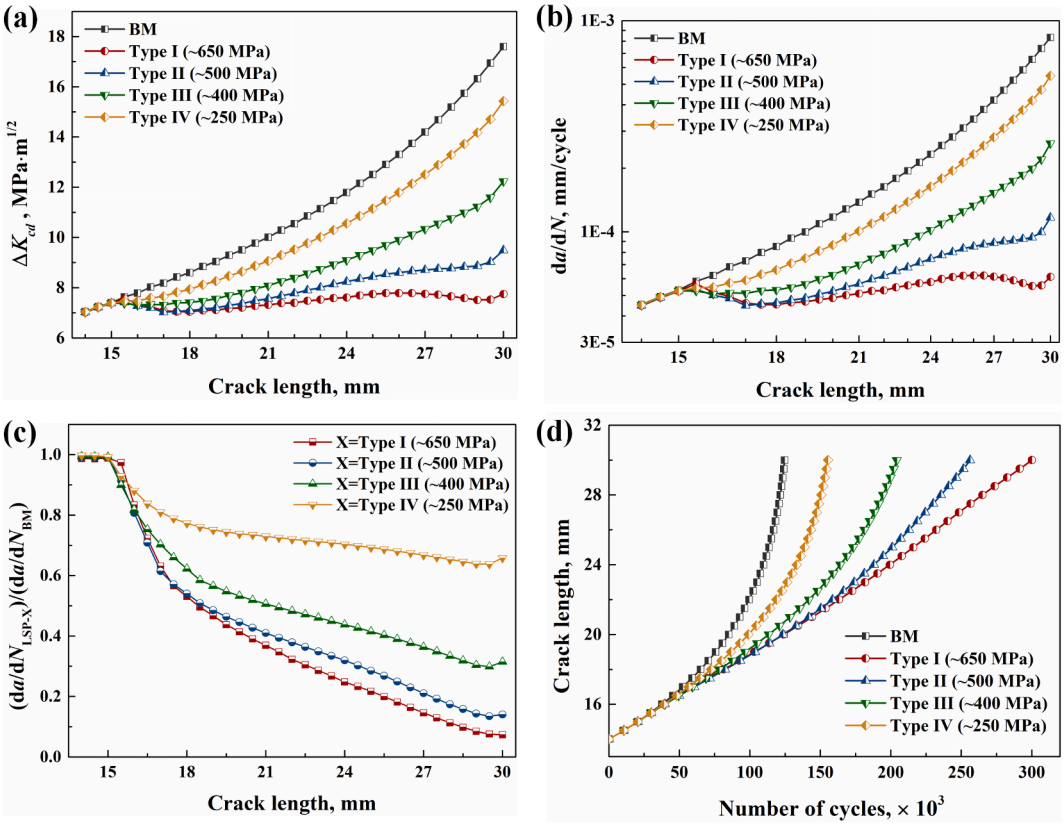

Fig. 12. SIF range ΔK_{cd} and FCP rate da/dN, depending on the crack length for the different compressive residual stress magnitudes, are displayed in (a) and (b), respectively. The resulting FCP retardation related to the FCP rate of the base material ($da/dN_{LSP,X_i}$: da/dN_{BM}) is shown in (c). Finally, the resulting number of load cycles is given in (d).

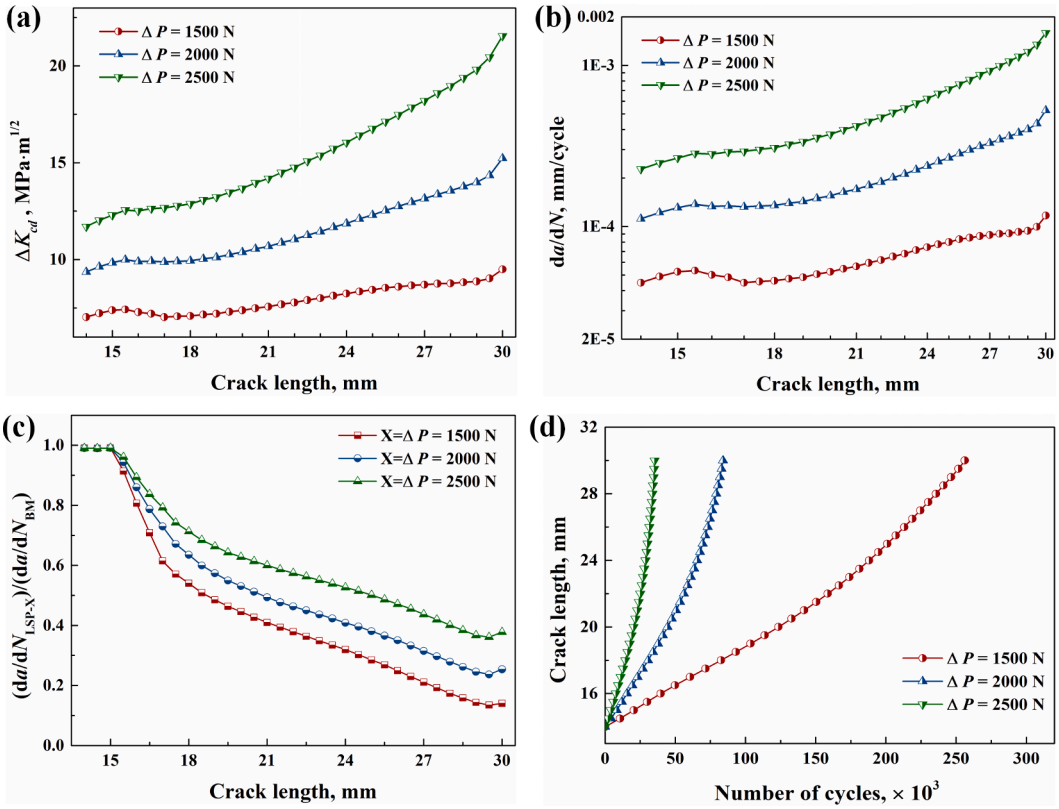

Fig. 13. Simulated FCP behavior in the specimens for different applied load ranges ΔP at a constant load ratio of 0.1. (a) depicts the SIF ranges under combined loading of applied and residual stresses ΔK_{cd} and (b) the resulting da/dN over crack length. (c) shows the FCP retardation ($da/dN_{LSP,X_i}$: da/dN_{BM}) related to the FCP rate of the base material. The resulting number of load cycles depending on the different load range is given in (d).

Tensile residual stresses between the initial crack front and the peened area even lead to an accelerated FCP rate. Predicting this effect requires considering the SIF ratio in the FCP equation, since tensile residual stresses lead to a superposition of the SIF and do not change the SIF range. Paris's law does not account for the SIF ratio, and therefore the use of other FCP laws, such as the NASGRO equation is required. However, for the sake of brevity, this effect is not further discussed in this study, and the interested reader is referred to Keller et al. [31].

4.3.2. *Influence of the maximum of introduced residual stress*

Significant retardation occurs when crack closure is present; this effect is expected to be influenced by the magnitude of the residual stresses, since higher compressive residual stress values are expected to lead to higher applied forces at which crack closure occurs. In this regard, the influence of the maximum compressive residual stress value on the FCP is investigated numerically in this section. For this purpose, the eigenstrain method is used to introduce step-wise constant residual stress distributions into the C(T) specimens, as shown in Fig. 11, where Type II, with a maximum of 500 MPa, corresponds to the eigenstrain approximation corresponding to the experimental results in Section 4.2, see Fig. 6.

The resulting SIF ranges ΔK_{cd} and FCP rates da/dN are presented in Fig. 12 for the respective residual stress fields. All investigated residual stress fields lead to an FCP retardation; however, there are significant differences. While ΔK_{cd} and da/dN increase with an increasing crack length for the investigated residual stress fields Types II-IV, Type I leads even to a slight decrease in these quantities, see $a = 27$ mm to $a = 29$ mm in Fig. 12a-b. The significant differences in the propagation rates indicate that high compressive residual stresses are a key factor for the retardation of fatigue cracks. The underlying mechanism is crack closure during the fatigue load cycles [32]. The increased magnitude of the compressive residual stresses influences the amount of crack closure and the applied force at which crack closure occurs. The FCP retardation in Fig. 12c demonstrates that significant retardation occurs when the residual stress increases from 250 MPa to 400 MPa for the crack length 16 mm $< a <$ 30 mm; however, only a relatively small increase in retardation is achieved when the residual stress magnitudes of 500 MPa and 650 MPa at 16 mm $< a <$ 21 mm are compared. Thereafter, the retardation of the FCP increases with increasing crack length for $a >$ 21 mm, comparing the influence of the residual stress magnitudes of 500 MPa and 650 MPa. This observation is explained by crack closure, which is significantly different for residual stress magnitudes of 250 MPa and 400 MPa along the whole crack length, but similar between 500 MPa and 650 MPa at 16 mm $< a <$ 21 mm.

The resulting number of load cycles for the mentioned residual stress magnitudes are shown in Fig. 12d. The increase in the maximum compressive residual stress always leads to an increased cycle number until the final crack length $a = 30$ mm is reached. However, there is no significantly increased load cycle number between Types I and II for the crack length range 16 mm $< a <$ 21 mm. This follows the observation of the marginally different FCP retardation mentioned earlier. However, it indicates that the fatigue life improvement after LSP might differ depending on the current crack length.

4.3.3. *Influence of the magnitude of the applied loads*

Fig. 13 shows ΔK_{cd} and da/dN as a function of the crack length under different applied load ranges, namely 1.5 kN, 2 kN, and 2.5 kN[1], at a constant stress ratio of 0.1. ΔK_{cd} increases with crack length under all three applied loads, corresponding to the constant amplitude test condition. However, with increasing applied load range, the retardation of the fatigue crack propagation is reduced, showing the lower effect of the residual stresses for higher applied load ranges. As the overall load range is increased by

[1] Corresponding to maximum forces of 1.67 kN, 2.22 kN, and 2.78 kN.

increasing the maximum force, the load range without the occurrence of crack closure is increased as well, i.e. the load range between the minimum force that completely opens the crack and the maximum applied force. Therefore, the relative reduction in ΔK_{cd} by residual stresses compared to residual stress free material is lower, when the maximum applied force is high and opens the crack completely. The significance of the externally applied loads on the fatigue life is demonstrated by integrating the da/dN, see Fig. 13d. An increase in the applied load range by increasing the maximum load significantly reduces the total fatigue life.

Compressive residual stresses need to be high enough to cause crack closure that reduces the SIF range and to cause significant FCP retardation. For a constant load ratio, an increased load range leads to an increased mean stress of the applied load cycles. Thus, compressive residual stresses need to be higher for an increased load range when the load ratio is kept constant to cause the same FCP retardation as for lower load ranges. These observations show that the application of LSP needs also to be adjusted to the present applied load range.

5. Conclusions

This article presents a combined experimental-numerical study of the fatigue crack retardation in a Ti-17 titanium alloy. LSP experiments are conducted to introduce characteristic residual stress fields, which are experimentally determined by incremental hole drilling. A multi-step simulation scheme is applied, containing the LSP process simulation by FE analysis, the SIF calculation affected by residual stresses and crack closure, the calculation of the FCP rate, as well as the total load cycle number. The main findings can be summarized as follows:

(1) Significant compressive residual stresses have been introduced to Ti-17 C(T) specimens up to a depth of 0.8 mm, and consequently, fatigue crack retardation has been experimentally observed. The fatigue life is increased by more than 150% at the crack length of 30 mm compared to unpeened specimens.

(2) The experimentally validated multi-step simulation comprises four steps: (i) LSP process simulation, (ii) plastic strain transfer, (iii) residual stress and SIF prediction, and (iv) FCP rate calculation and integration. The simulation approach successfully predicts the fatigue crack retardation compared to the untreated material.

(3) Crack closure is the main mechanism for fatigue crack retardation in Ti-17 titanium alloy, which is consistent with the reported investigation on aluminum. The crack closure is indicated based on numerical simulations and SEM images of the fracture surfaces in the regions of high compressive residual stresses. These results suggest a cross-material explanation for the fatigue crack retardation caused by the LSP treatment due to crack closure.

(4) The generation of fatigue crack retardation results from combined influences of an appropriate LSP design. The numerical investigation indicates that high values of compressive residual stresses and a small peening patch distance are beneficial with regard to fatigue life extension. However, the efficiency of the LSP application depends heavily on the external loading that has to be considered in terms of the LSP design as well.

Declaration of Competing Interest

The authors declare that they have no known competing financial interests or personal relationships that could have appeared to influence the work reported in this paper.

Acknowledgment

The authors would like to acknowledge the support for this work of research from the Key Laboratory Funding for Equipment Pre-research (Grant No. JZX7Y201911SY008601) and the Aeronautical Science Foundation of China (Grant No. 20185425009). The authors also acknowledge the support provided by the China Scholarship Council (CSC) during the visit of Rujian Sun at Helmholtz-Zentrum Geesthacht.

Appendix A. Convergence study of the eigenstrain approach in terms of residual stresses and SIFs

The Appendix provides a brief comment on the averaging volumes of the eigenstrain approach and a respective convergence study. Residual stresses determined by the eigenstrain method within the C(T) specimen for different averaging volumes are shown in Fig. A1. The volume sizes, i.e. 0.25 mm, 0.125 mm, and 0.0625 mm, are in the material thickness direction. The introduced residual stress distribution shows a step-wise characteristic depending on the averaging volume size of the plastic strains (Step II of the multi-step simulation). It is obvious that smaller averaging volumes lead to higher maximum values of the volume-averaged plastic strain, resulting in higher strain gradients and higher residual stresses. It is also worth noting that the residual stresses exhibit some distortion on the first peened side when a smaller element size is employed, leading to a higher residual stress resolution in the material thickness direction. This might be influenced by the stress-hole effect related to the phenomenon that the maximum compressive residual stress is located neither on the surface nor at the center, but at the subsurface in the depth direction, or in the area slightly off the center; however, the real reason remains to be ascertained [49].

Fig. A2 shows the simulated K_{cd} values and ΔK_{cd} for the C(T) specimen as a function of the crack length for different averaging volume sizes in the depth direction. One can observe that the averaging volume size in the depth direction has no significant influence on the K_{cd} value, indicating that

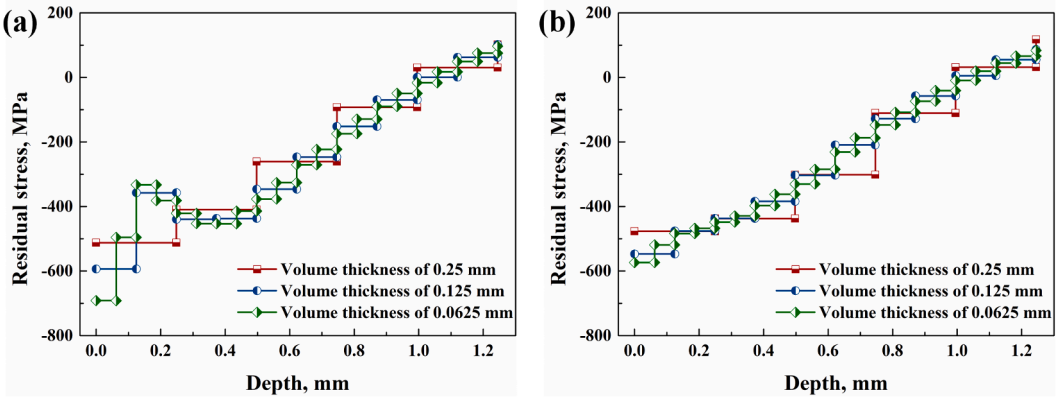

Fig. A1. Residual stress distribution on the C(T) specimen with different element sizes. (a) 1st LSP-treated side and (b) 2nd LSP-treated side.

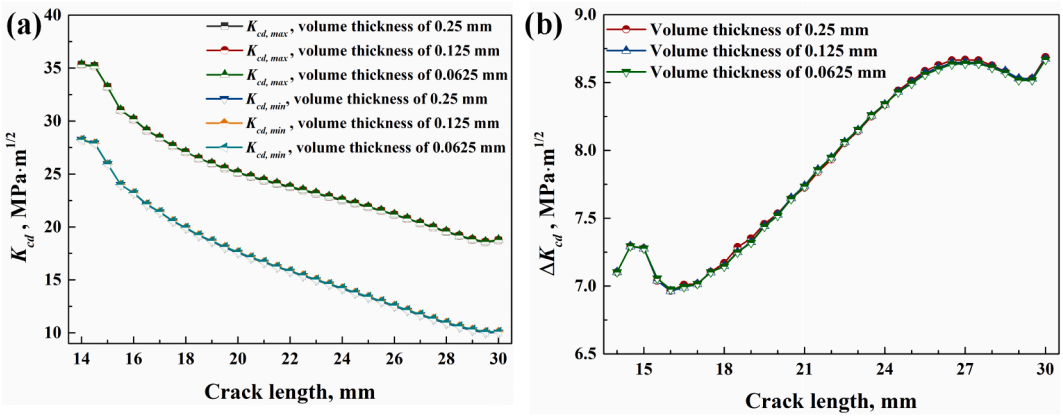

Fig. A2. Comparison of simulated K_{cd} (a) and ΔK_{cd} (b) values with different averaging volume sizes in the depth direction.

every investigated volume size gives accurate SIF results for the present load and residual stress case. Therefore, the element size of 0.25 mm, which is used for the FCP simulations in this works, leads to converged SIF predictions.

References

[1] Leyens C, Peters M. Titanium and Titanium Alloys: Fundamentals and Applications. John Wiley & Sons; 2003.
[2] Boyer R. An overview on the use of titanium in the aerospace industry. Mater. Sci. Eng., A 1996;213:103–14.
[3] Peters M, Kumpfert J, Ward CH, Leyens C. Titanium alloys for aerospace applications. Adv. Eng. Mater. 2003;5:419–27.
[4] Boyer R, Briggs R. The use of β titanium alloys in the aerospace industry. J. Mater. Eng. Perform. 2005;14:681–5.
[5] Chen C, Ye D, Zhang L, Liu J. Effects of tensile/compressive overloads on fatigue crack growth behavior of an extra-low-interstitial titanium alloy. Int. J. Mech. Sci. 2016;118:55–66.
[6] Huang X, Neu R. High-load fretting of Ti–6Al–4V interfaces in point contact. Wear 2008;265:971–8.
[7] Hua Y, Bai Y, Ye Y, Xue Q, Liu H, Chen R, et al. Hot corrosion behavior of TC11 titanium alloy treated by laser shock processing. Appl. Surf. Sci. 2013;283:775–80.
[8] Lin B, Lupton C, Spanrad S, Schofield J, Tong J. Fatigue crack growth in laser-shock-peened Ti–6Al–4V aerofoil specimens due to foreign object damage. Int. J. Fatigue 2014;59:23–33.
[9] Peters J, Ritchie R. Influence of foreign-object damage on crack initiation and early crack growth during high-cycle fatigue of Ti–6Al–4V. Eng. Fract. Mech. 2000;67:193–207.
[10] Nowell D, Duo P, Stewart I. Prediction of fatigue performance in gas turbine blades after foreign object damage. Int. J. Fatigue 2003;25:963–9.
[11] Liu J, Yuan H, Liao R. Prediction of fatigue crack growth and residual stress relaxations in shot-peened material. Mater. Sci. Eng. A – Struct. Mater. Properties Microstruct. Process. 2010;527:5962–8.
[12] Rios ERDL, Walley A, Milan MT, Hammersley G. Fatigue crack initiation and propagation on shot-peened surfaces in A316 stainless steel. Int. J. Fatigue 1995;17:493–9.
[13] Regazzi D, Beretta S, Carboni M. An investigation about the influence of deep rolling on fatigue crack growth in railway axles made of a medium strength steel. Eng. Fract. Mech. 2014;131:587–601.
[14] Munoz-Cubillos J, Coronado JJ, Rodriguez SA. Deep rolling effect on fatigue behavior of austenitic stainless steels. Int. J. Fatigue 2017;95:120–31.
[15] Ge M-Z, Xiang J-Y. Effect of laser shock peening on microstructure and fatigue crack growth rate of AZ31B magnesium alloy. J. Alloy Compd. 2016;680:544–52.
[16] Bergant Z, Trdan U, Grum J. Effects of laser shock processing on high cycle fatigue crack growth rate and fracture toughness of aluminium alloy 6082–T651. Int. J. Fatigue 2016;87:444–55.
[17] Tan Y, Wu G, Yang JM, Pan T. Laser shock peening on fatigue crack growth behaviour of aluminium alloy. Fatigue Fract. Eng. Mater. Struct. 2010;27:649–56.
[18] Cuellar SD, Hill MR, Dewald AT, Rankin JE. Residual stress and fatigue life in laser shock peened open hole samples Servando D. Cuellar. Int. J. Fatigue 2012;44:8–13.
[19] Sun R, Li L, Zhu Y, Guo W, Peng P, Cong B, et al. Microstructure, residual stress and tensile properties control of wire-arc additive manufactured 2319 aluminum alloy with laser shock peening. J. Alloy. Compd. 2018;747:255–65.
[20] Guo W, Sun R, Song B, Zhu Y, Li F, Che Z, et al. Laser shock peening of laser additive manufactured Ti6Al4V titanium alloy. Surf. Coat. Technol. 2018;349:503–10.
[21] Achintha M, Nowell D. Eigenstrain modelling of residual stresses generated by laser shock peening. J. Mater. Process. Technol. 2011;211:1091–101.
[22] Ding K, Ye L. Laser shock peening: performance and process simulation. Woodhead Publishing; 2006.
[23] Zhou J, Huang S, Zuo L, Meng X, Sheng J, Tian Q, et al. Effects of laser peening on residual stresses and fatigue crack growth properties of Ti–6Al–4V titanium alloy. Opt. Lasers Eng. 2014;52:189–94.
[24] Yang Y, Zhou W, Chen B, Tong Z, Chen L, Ren X. Fatigue behaviors of foreign object damaged Ti-6Al-4V alloys under laser shock peening. Int. J. Fatigue 2020;136:105596.
[25] Zhao J, Dong Y, Ye C. Laser shock peening induced residual stresses and the effect on crack propagation behavior. Int. J. Fatigue 2017;100:407–17.
[26] van Aswegen D, Polese C. Experimental and analytical investigation of the effects of laser shock peening processing strategy on fatigue crack growth in thin 2024 aluminium alloy panels. Int. J. Fatigue 2020;142:105969.
[27] Kashaev N, Ventzke V, Horstmann M, Chupakhin S, Riekehr S, Falck R, et al. Effects of laser shock peening on the microstructure and fatigue crack propagation behaviour of thin AA2024 specimens. Int. J. Fatigue 2017;98:223–33.
[28] Hu Y, Cheng H, Yu J, Yao Z. An experimental study on crack closure induced by laser peening in pre-cracked aluminum alloy 2024–T351 and fatigue life extension. Int. J. Fatigue 2020;130:105232.
[29] Pavan M, Furfari D, Ahmad B, Gharghouri M, Fitzpatrick M. Fatigue crack growth in a laser shock peened residual stress field. Int. J. Fatigue 2019;123:157–67.
[30] Busse D, Ganguly S, Furfari D, Irving PE. Optimised laser peening strategies for damage tolerant aircraft structures. Int. J. Fatigue 2020;141:105890.
[31] Keller S, Horstmann M, Kashaev N, Klusemann B. Experimentally validated multi-step simulation strategy to predict the fatigue crack propagation rate in residual stress fields after laser shock peening. Int. J. Fatigue 2019;124:265–76.
[32] Keller S, Horstmann M, Kashaev N, Klusemann B. Crack closure mechanisms in residual stress fields generated by laser shock peening: A combined experimental-numerical approach. Eng. Fract. Mech. 2019;221:106630.
[33] Sun R, Li L, Guo W, Peng P, Zhai T, Che Z, et al. Laser shock peening induced fatigue crack retardation in Ti-17 titanium alloy. Mater. Sci. Eng., A 2018;737:94–104.
[34] Chupakhin S, Kashaev N, Huber N. Effect of elasto-plastic material behaviour on determination of residual stress profiles using the hole drilling method. J. Strain Analy. Eng. Des. 2016;51:572–81.
[35] Saxena A, Hudak SJ. Review and extension of compliance information for common crack growth specimens. Int. J. Fract. 1978;14:453–68.
[36] Steinzig M, Ponslet E. Residual stress measurement using the hole drilling method and laser speckle interferometry: part 1. Exp. Tech. 2003;27:43–6.
[37] Ponslet E, Steinzig M. Residual stress measurement using the hole drilling method and laser speckle interferometry. Part II: Analy. Tech., Exp. Tech. 2003;27:17–21.
[38] Steinzig M, Takahashi T. Residual stress measurement using the hole drilling method and laser speckle interferometry Part IV: Measurement accuracy. Exp. Tech. 2003;27:59–63.
[39] Ponslet E, Steinzig M. Residual stress measurement using the hole drilling method and laser speckle interferometry Part III: Analysis technique. Exp. Tech. 2003;27:45–8.
[40] Korsunsky AM, Regino GM, Nowell D. Variational eigenstrain analysis of residual stresses in a welded plate. Int. J. Solids Struct. 2007;44:4574–91.
[41] Jun T-S, Korsunsky AM. Evaluation of residual stresses and strains using the Eigenstrain Reconstruction Method. Int. J. Solids Struct. 2010;47:1678–86.
[42] Johnson GR, Cook WH. A constitutive model and data for metals subjected to large strains, high strain rates and high temperatures. Eng. Fract. Mech. 1983;21:541–8.
[43] Wang B, Xing AI, Liu Z, Liu J. Plastic Flow Modeling of Ti-SAI-2Sn.2Zr-4Mo-4Cr Alloy at Elevated Temperatures and High Strain Rates. J. Wuhan Univ. Technol. 2015;161:611–6.
[44] Keller S, Chupakhin S, Staron P, Maawad E, Kashaev N, Klusemann B. Experimental and numerical investigation of residual stresses in laser shock peened AA2198. J. Mater. Process. Technol. 2018;255:294–307.

[45] Krueger R. Virtual crack closure technique: History, approach, and applications. Appl. Mech. Rev. 2004;57:109–43.
[46] Okada H, Kamibeppu T. A Virtual Crack Closure-Integral Method (VCCM) for Three-Dimensional Crack Problems Using Linear Tetrahedral Finite Elements. Cmes-computer Model. Eng. Sci. 2005;10:229–38.
[47] Paris PC. A rational analytic theory of fatigue. Trend Eng. 1961;13:9.
[48] King A, Steuwer A, Woodward C, Withers P. Effects of fatigue and fretting on residual stresses introduced by laser shock peening. Mater. Sci. Eng., A 2006;435:12–8.
[49] Hu Y, Yao Z, Wang F, Hu J. Study on residual stress of laser shock processing based on numerical simulation and orthogonal experimental design. Surf. Eng. 2007;23:470–8.